nature astronomy

Article

https://doi.org/10.1038/s41550-026-02928-0

On the coronal origin of magnetic switchbacks in the solar wind

Received: 9 August 2024

Accepted: 17 June 2026

Published online: 8 October 2026

Check for updates

Jesse T. Coburn[1,2] ✉, Stephanie L. Yardley[1,3,4], Nawin Ngampoopun[1,5], Ryan Dewey[6], Yeimy J. Rivera[7], Rossana De Marco[8], Daniel Verscharen[1], Christopher J. Owen[1], Gabriel H. H. Suen[9], Benjamin Alterman[10], Deborah Baker[1], Andrew Fazakerley[1], Antoinette B. Galvin[11], Jiansen He[12], Timothy S. Horbury[13], Chuanpeng Hou[12,14], Charalambos Ioannou[1], Lynn M. Kistler[11], Susan T. Lepri[6], Stefano Livi[6,15], Philippe Louarn[16], Georgios Nicolaou[1], Jim M. Raines[6] & Alexis P. Rouillard[17,18]

The Sun continuously releases a stream of charged particles known as the solar wind, threaded by magnetic field lines that occasionally fold back on themselves in sharp reversals called magnetic switchbacks. These structures are frequently observed by spacecraft near the Sun, but their formation mechanism remains an open question. Using measurements from Solar Orbiter at 0.55 AU, we report heavy ion observations within a magnetic switchback that provide direct evidence of its solar source. Elevated charge-state ratios of oxygen and carbon, combined with a depletion of helium relative to protons, indicate that the switchback plasma originated from hot, closed coronal loop structures. A semi-empirical coronal model, constrained by electron temperature and density measurements from the Solar Dynamics Observatory, traces the ion signatures to either a coronal hole boundary or loops within the coronal hole, implicating the source mechanism as interchange reconnection, where closed loops reconnect with open magnetic field and eject plasma. The proton velocity and magnetic field fluctuations of the switchback are in accordance with an outward-propagating Alfvén wave. These findings suggest that interchange reconnection and wave or turbulence mechanisms jointly govern switchback origin and propagation, respectively. Most importantly, we show that switchbacks preserve measurable signatures, carrying information about the physical processes that heat the solar atmosphere and accelerate the solar wind.

There are two main paradigms capable of describing the processes that heat the solar atmosphere and accelerate the solar wind: waves and turbulence, or reconnection[1]. A consistent comparison between the aforementioned theories of the solar atmosphere and observations is obscured by the drastic changes in density and temperature, for example, the transition region. The solar atmosphere exhibits a span of plasma regimes: partially ionized to fully ionized, collisional to nearly collisionless, closed to open magnetic field, and the dominant electromagnetic emission changes from collisional excitation to resonant scattering. This isolates the utility of the observational techniques and theoretical descriptions[2]. We present observations of heavy ions (atomic mass number greater than 1) by the European Space Agency (ESA)/National Aeronautics and Space Administration (NASA) Solar Orbiter spacecraft[3] that provide a clear link between the solar atmosphere and the solar wind.

These observations provide sufficient evidence to identify the solar source of a magnetic switchback, a class of interplanetary

A full list of affiliations appears at the end of the paper. ✉e-mail: jesse.coburn@lpp.polytechnique.fr

magnetic field (IMF) reversal. IMF reversals are observed over a wide range of spatiotemporal scales; some examples include small-scale flux ropes[4–6], reconnection between open–closed magnetic field (that is, interchange reconnection[7,8]), interplanetary coronal mass ejections[7,9] and the heliospheric current sheet[10]. While some IMF reversals correspond to a change in sector polarity, that is, a change in coronal connectivity, many IMF reversals do not (see ref. 11 for an early observation). The direction of the suprathermal electron beam can reveal the polarity of the IMF (see ref. 12 for a review), providing information on key heliospheric processes.

Small-scale magnetic field reversals are rarely a true change in sector polarity; typically, they are large-amplitude Alfvén-like fluctuations[13]. Indeed, observations of the polarity of solar-wind ion velocity and magnetic field fluctuations are consistent with outward-propagating Alfvén-like structures[14,15], a key indicator of magnetic switchbacks. Parker Solar Probe has indicated that the occurrence rate of magnetic switchbacks is higher in the near-Sun region[16–22]. The possibility that they retain information about their coronal origin[23] is hinted at by the modulation of the switchback amplitude on the scale of the super-granular size[24], the radial occurrence rate[25] and the statistics of their elemental composition[26–28].

Whether switchbacks provide information about coronal processes is a particularly compelling question owing to the dichotomy between candidate generation mechanisms. There is support for generation by interchange reconnection[8,29–34], and by waves and turbulence, for example, velocity shears[35] or expansion of Alfvén-like turbulence[36–39]. The division in switchback generation mechanisms, that is, reconnection versus waves and turbulence, is analogous to the division of candidate mechanisms that can explain coronal heating and solar wind acceleration[40].

Results

Tracing the magnetic field from Solar Orbiter to the Sun

We analyse in situ observations by Solar Orbiter on 2 March 2022 and model the coronal and interplanetary magnetic field to identify the source region of the plasma. Figure 1 shows the magnetic-field footpoint predictions, coloured by the inferred in situ observation time. These are interpreted as the magnetic field lines that connect between Solar Orbiter and the Sun during the interval. We discuss caveats and the trustworthiness of these footpoints in 'The magnetic field model' section in Methods. We show the footpoint predictions based on two assumed source surface heights. The larger source surface height ($2.5R_{\rm Sun}$) is marked by squares that have an area proportional to the probability of connection based on the tool developed by the Institut de Recherche en Astrophysique et Planétologie (IRAP) ('The magnetic-field model' section in Methods)[41]. The second set of magnetic field footpoint predictions, denoted by coloured circles, are calculated with an assumed source surface height of $2R_{\rm Sun}$ (refs. 42,43).

Near the end of 1 March 2022, the footpoint predictions lie at the boundary of an active region (see the black–yellow colour bar) in the northern hemisphere; later, the prediction is along the edge of a coronal hole (that is, the dark region inside the black contour), and then at the boundary of another active region in the southern hemisphere.

The background colour is the observation by Solar Dynamics Observatory's (SDO) Atmospheric Imaging Assembly (AIA), which is proportional to the emission intensity, in the 193-Å wavelength filter band, in units of digital number (dn), is dominated by emission from excited states of Fe (ref. 44). The emission intensity is further analysed to provide the electron temperature and density of the source region by employing the differential emission measure (DEM) technique ('SDO measurements and the DEM' section in Methods). Figure 1 shows a 1.2-MK contour, in black, of the coronal electron temperature.

During the time span of Fig. 1, the inferred solar source changes between coronal hole and active region boundaries[43], encompassing a period when the predicted magnetic field lines connect to a coronal hole. With Solar Orbiter, we observe (in situ) intermittent switchbacks in this period. We focus our in situ observations on the 6-h period denoted by the vertical white bars in the multi-colour bar of Fig. 1.

The magnetic switchback as observed by Solar Orbiter

Figure 2 displays high-resolution in situ observations recorded by Solar Orbiter while the spacecraft was at approximately 0.55 AU (~120 solar radii). Figure 2a shows the electron pitch angle (α) distribution averaged over energies from 60 eV to 1,000 eV, where $\alpha = \arccos\{v_\parallel/|\mathbf{v}|\}$; $\mathbf{v}$ is the electron velocity and $v_\parallel$ is the component of the electron velocity parallel to the local magnetic field $\mathbf{B}$. Throughout most of the interval, the maximum phase space density is near to α=180°, which is a signature of the suprathermal electron beam that travels away from the Sun along the magnetic field. Therefore, during this interval, the sector polarity of the magnetic field remains Sunward.

During five intervals, which we shade in yellow, the radial component of the magnetic field (shown as a red line in Fig. 2b) reverses to the anti-Sunward direction. In these periods, the maximum of the suprathermal electron pitch angle distribution, in units of phase space density (PSD), remains near α=180°, indicating that these magnetic field reversals are switchbacks[16,22]. Figure 2c shows three solar wind heavy ion charge-state number density ratios $n_{O^{7+}}/n_{O^{6+}}$, $n_{C^{6+}}/n_{C^{4+}}$ and $n_{C^{6+}}/n_{C^{5+}}$ that increase cotemporally with the major switchback spanning 20:25:00 to 21:55:00 UTC.

Figure 2d shows the radial bulk speeds u_R of the ions O^{6+}, O^{7+} and He^{2+} and protons u_R^p, where the latter increases comparably to the local radial Alfvén speed $u_R^{Alfvén} = B_R/\sqrt{4\pi(n_p + 4n_{He^{2+}})m_p}$ inside the switchbacks. $\langle\ldots\rangle_\tau$ is a moving average of time length τ ('Analysis of particle distribution function measurements' section in Methods). The relative speed difference between the heavy ions and the protons (for example, $u_R^p - \langle u_R^{He^{2+}}\rangle_{100s}$) changes sign in the switchback periods, indicating that there is no change in the sector polarity of the magnetic field, consistent with the suprathermal electron pitch angle distribution in Fig. 2a. In addition, the magnitude of the speed differences (for example, $u_R^p - \langle u_R^{He^{2+}}\rangle_{100s}$) for all heavy ions is less than the local radial Alfvén speed (Fig. 2d, grey line). Figure 2e compares the proton temperature T_p with the heavy ion temperatures divided by their atomic mass number. Inside and outside of the switchbacks, the temperatures of the heavy ions are larger than temperature–mass proportionality, relative to the protons, for example, $\langle T_{O^{6+}}\rangle_{30s}/T_p \propto 16$. The grey line of $T_p \times 1.8$ demonstrates the super-mass proportionality and is respective to the temperatures we observe in this interval. Figure 2f presents moving averages of three quantities we interpret as identifiers of solar source: the solar wind electron temperature T_e and the two number density ratios $n_{He^{2+}}/n_p$ and $n_{O^{7+}}/n_{O^{6+}}$. In this panel, we use high-resolution measurements of $n_{O^{7+}}/n_{O^{6+}}$. T_e and $n_{O^{7+}}/n_{O^{6+}}$ are correlated, and anti-correlated with $n_{He^{2+}}/n_p$. Local and respective to the time scale of each switchback, T_e and $n_{O^{7+}}/n_{O^{6+}}$ increase and $n_{He^{2+}}/n_p$ decreases.

Diagnosing the source region with a semi-empirical model

We further analyse the ion charge-state ratios by building a semi-empirical model of the corona ($1.06R_{\rm Sun} < R \lesssim 5R_{\rm Sun}$) to predict the freeze-in charge-state ratios for comparison with observations by Solar Orbiter. This follows a similar method constructed in ref. 45. We use the DEM technique to obtain measurements of the most probable electron temperature $\bar{T}_e$ and density $\bar{n}_e$ ('SDO measurements and the DEM' section in Methods) of the low corona $R \approx 1.06R_{\rm Sun}$, which we present in Fig. 3. We focus on $\bar{T}_e$ by drawing three filled contours (green, blue and magenta) that span $[\bar{T}_e - \sigma_{\bar{T}_e}, \bar{T}_e + \sigma_{\bar{T}_e}]$. The errors for the temperature $\sigma_{\bar{T}_e}$ are shown relative to the most probable values in Fig. 3c. We show the density $\bar{n}_e$ and relative error $\sigma_{\bar{n}_e}/\bar{n}_e$ in Fig. 3b,d.

https://doi.org/10.1038/s41550-026-02928-0

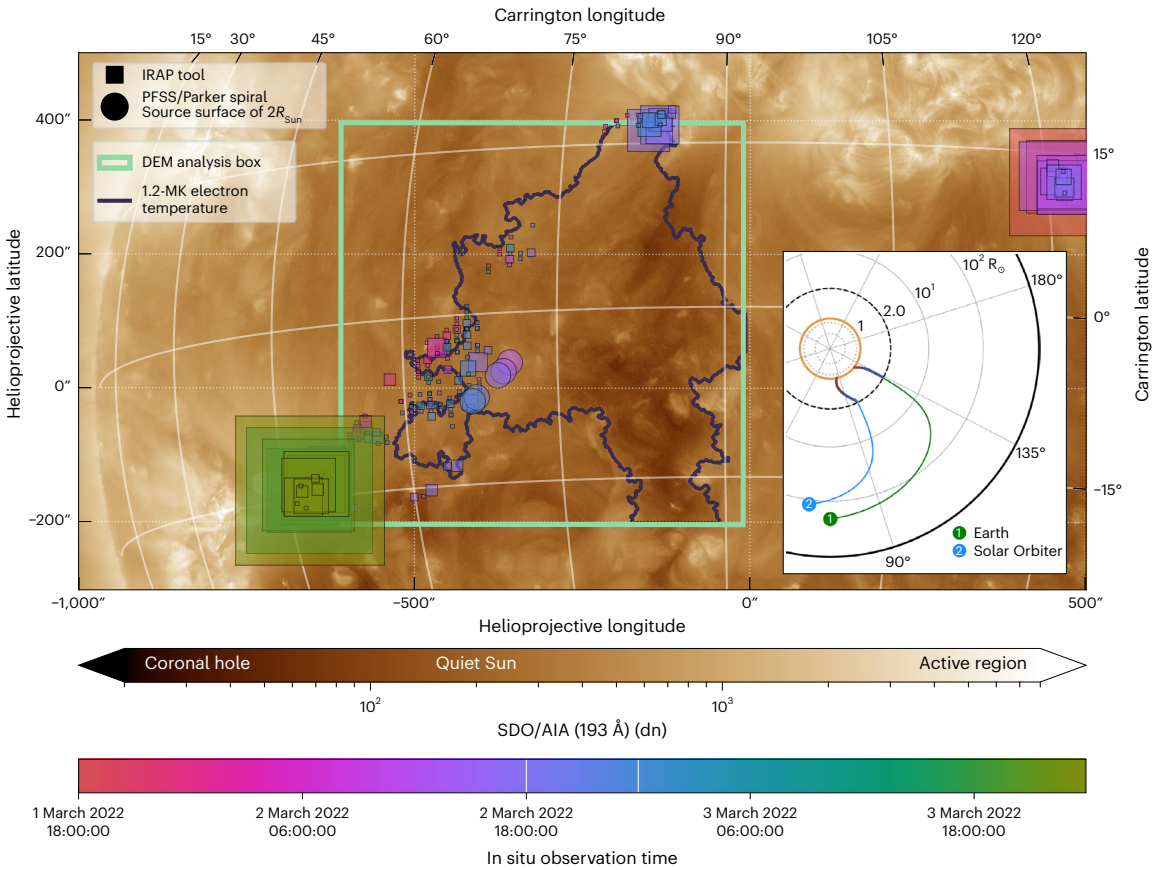


Fig. 1 | The solar source and magnetic footpoints during the event. SDO/AIA observation of extreme ultraviolet emission intensity in the 193-Å wavelength passband (see 'SDO measurements and the DEM' section in Methods for discussion). The observation was made on 28 February 2022 at 12:30 (HH:MM) UTC. We show footpoint predictions of magnetic field lines that connect from Solar Orbiter to the Sun. The white frame inset shows how the position of Solar Orbiter and Earth (approximately the location of SDO) connect by Parker's spiral for radius $\geq 2R_{Sun}$ and the potential field source surface (PFSS) model for radius $<2R_{Sun}$. The inset is shown for the middle of the day on 2 March 2022 in the time frame 'In situ observation time'. Notice that SDO can view the portion of the Sun where Solar Orbiter is predicted to be connected. The magnetic field footpoint predictions are shown for the IRAP model from ref. 41 and for a source surface height of $2R_{Sun}$ (upper left legend) over a time span that we indicate by the 'In situ observation time' colour bar, in which two vertical white lines denote the time span of the in situ analysis shown in Fig. 2. The green box indicates the region where we employ the DEM technique to obtain the coronal electron temperature and density. The 1.2-MK electron temperature contour is shown in black.

The $\bar{n}_e$ and $\bar{T}_e$ observations are set as the lower boundary condition of the semi-empirical coronal model.

Figure 4a,b shows the results from the numerical simulation in ref. 46 of the electron temperature and density in a coronal hole flux tube and the observations of a polar coronal hole in ref. 47. We construct the semi-empirical model by adjusting[46] the electron temperature and density profiles so that their lower boundary matches the values obtained from the DEM analysis. For example, the green curve in Fig. 3a corresponds to $T_e(R_{DEM}) = 1.2 \times 10^6$ K. The lower boundary of the green, blue and violet curves correspond with the colour bar of Fig. 3a. 'Charge-state ratio evolution in the corona' section in Methods explains the choice of $R_{DEM} = 1.06R_{Sun}$ and the R_{DEM} range.

To obtain the frozen-in charge-state ratios, we solve the non-equilibrium ionization equation ('Charge-state ratio evolution in the corona' section in Methods) based on coronal conditions, in particular, the electron temperature and density appears in Fig. 4a,b (refs. 48,49). The solutions for $n_{C^{6+}}/n_{C^{4+}}$, $n_{C^{6+}}/n_{C^{5+}}$ and $n_{O^{7+}}/n_{O^{6+}}$ given the ion speed, electron density and electron temperature profiles are shown in Fig. 4c–e. The width of the shaded regions shows the errors propagated from the uncertainty in the DEM analysis and the coronal model ('Charge-state ratio evolution in the corona' section in Methods).

The right panels in Fig. 4c–e show the in situ measurements by Solar Orbiter, which is at a distance of approximately $120R_{Sun}$. The peak of the reversal region of the switchback, shown as squares, corresponds to the peak value of the charge-state ratios of the major switchback region in Fig. 2c. The triangles are the average conditions from the non-reversal regions in Fig. 2c.

Figure 5 plots the three frozen-in charge-state ratios for each pixel shown in Fig. 3 according to the semi-empirical model presented in Fig. 4. The colour bars are bound by 1.25 times the peak charge-state ratio of the reversal region of the switchback (Fig. 4c–e, squares) and 0.75 times the average charge-state ratio conditions (Fig. 4c–e, triangles). The semi-empirical model, with the prescribed lower boundary conditions by the DEM analysis, provides a manner of mapping the solar source ion charge-state ratios to in situ observations.

In Fig. 5, the method of extrapolating the frozen-in charge-state ratio from the corona is extended to each pixel, with Fig. 5a–c corresponding to the three characteristic charge-state ratios. In each panel, we draw a select set of magnetic footpoints from Fig. 1 as blue/magneta circles which correspond to a source surface height of $2R_{Sun}$. White arrows point to three regions that our method indicates as charge-state enhanced. We assume that they are large magnetic loops inside the coronal hole and calculate the loop length by assuming they are semi-circle and constant-pressure structures ('Loop length estimate' section in Methods). We find loop lengths of approximately (13, 11, 18) arcsec, which is approximately (9.50, 7.97, 12.4) Mm, ranked in order of largest

https://doi.org/10.1038/s41550-026-02928-0

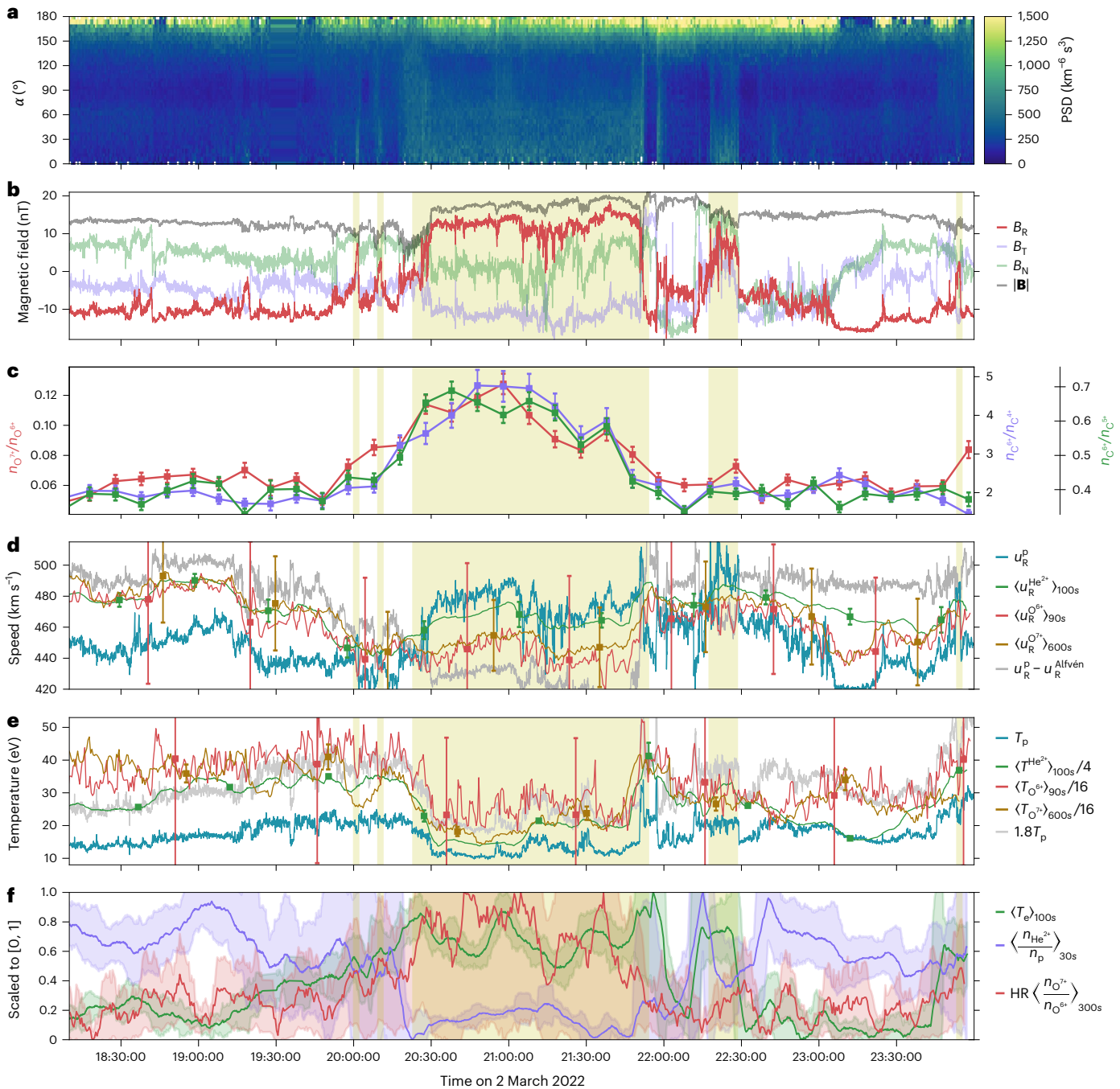


Fig. 2 | In situ measurements made by Solar Orbiter during a period containing magnetic switchbacks. We explain the measurements and the analysis, including the averages and errors, in 'In situ measurements of particles and fields' and 'Analysis of particle distribution function measurements' sections in Methods. **a**, The electron pitch angle distribution function averaged over electron energies of 60 eV to 1,000 eV. **b**, The magnetic field. **c**, Three ratios of charge states of characteristic heavy ions. **d**, The radial component of the velocity for a set of ions. The subscript on the angled brackets in the legends of **d**–**f** indicates the time span of a moving average. **e** The temperature of the ions, where the heavy ions have been normalized by their atomic mass number. **f**, Results scaled to the interval [0, 1] with the minimum and maximum of each quantity in the time interval. 'HR' in the legend of **f** indicates high-resolution data. The errors appear as capped bars in **c**–**e** and are shown as less opaque shading in **f** for visibility. Yellow shaded regions indicate periods of reversals of the radial magnetic field component.

to smallest helioprojective latitude[50–52]. The calculation of the loop lengths is consistent with the observed physical size of the structures, so we now refer to them as coronal hole loops.

Discussion

Figure 2 presents measurements of ion charge-state ratios during a switchback, providing sufficient information to determine the type of solar source of this switchback. We interpret the charge-state ratio enhancements (Fig. 2c) as evidence for elevated solar source temperature. The coronal ions undergo electron temperature- and density-dependent recombination and ionization near the Sun ($R \lesssim 5R_{Sun}$), which ceases where the density is low enough. As they escape, the charge state of the ions freezes in[48,49,53]. In general, higher coronal electron temperature corresponds to higher charge states.

We interpret the decrease in $n_{He^{2+}}/n_p$ (Fig. 2f) as evidence that the plasma in the major switchback originates from hot coronal loops. In

https://doi.org/10.1038/s41550-026-02928-0

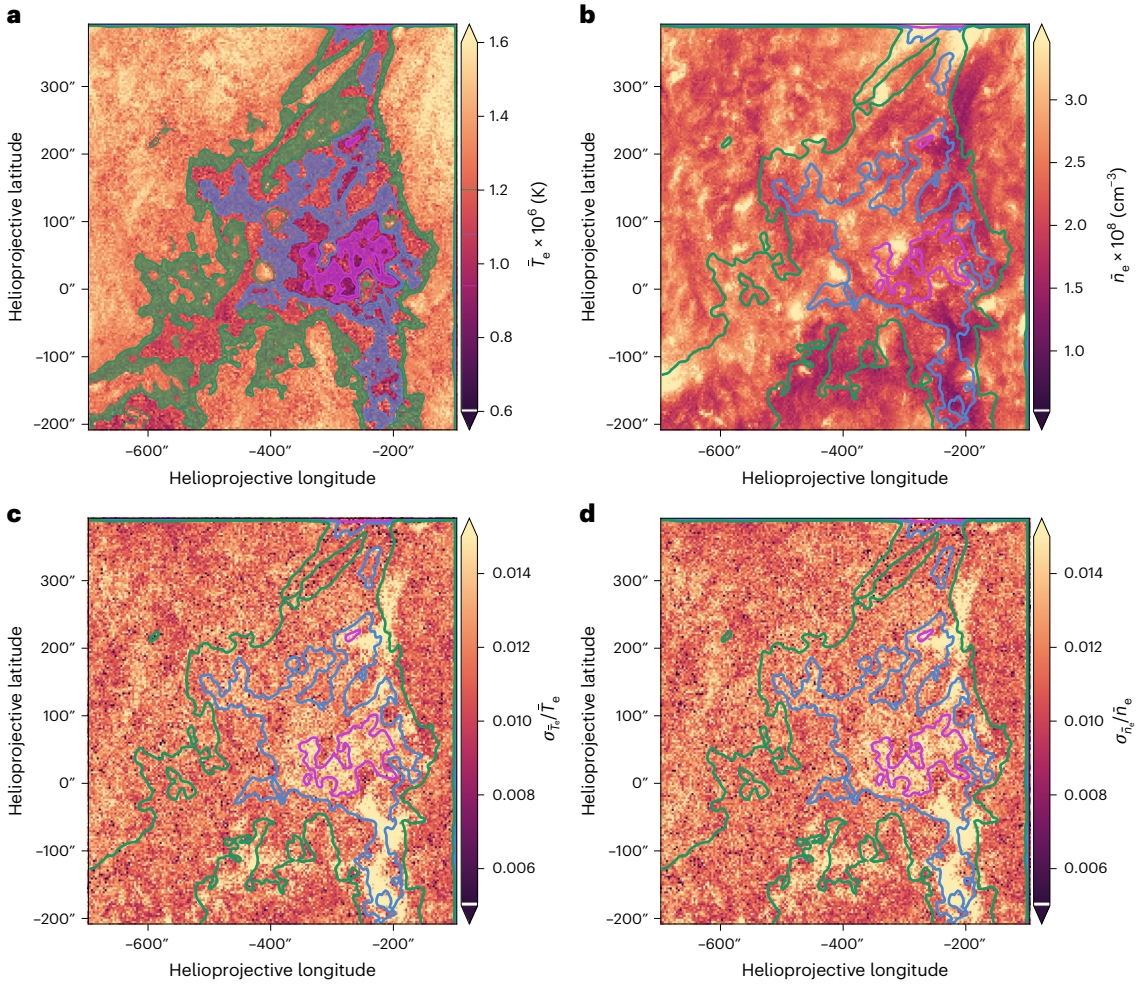


Fig. 3 | The most probable electron temperature and density of the coronal hole. a–**d**, The result of the DEM analysis ('SDO measurements and the DEM' section in Methods) for the most probable electron temperature (**a**), density (**b**) and the relative errors (**c** and **d**). The errors $\sigma_{\bar{T}_e}$, $\sigma_{\bar{n}_e}$ are propagated from the errors in the DEM quantity and temperature resolution ('SDO measurements and the DEM' section in Methods). The magenta, blue and green lines are contours of the electron temperature at $\bar{T}_e = (9.4 \times 10^5, 1.1 \times 10^6, 1.2 \times 10^6)$ K (see the colour bar in **a**). In **a**, we draw them as filled contours spanning $[\bar{T}_e - \sigma_{\bar{T}_e}, \bar{T}_e + \sigma_{\bar{T}_e}]$.

the chromosphere, the electron thermal energy exceeds the first ionization energy of the elements; transport is modified by local wave heating and inter-species collisions[54]. Since the wave heating on open and closed coronal magnetic field differs, the in situ measurement of ion abundance distinguishes the solar source[55–60].

Therefore, we claim that the mechanism that released this plasma is interchange reconnection[8,32]. There is substantial observational evidence indicating that the coronal plasma on closed-loop magnetic field is hotter than coronal plasma on open field[52]. This is supplemented by theory and simulations[61–63]. In addition, there is observational evidence for n_{He} depletion in the corona over quiet-Sun regions[64] and in the slow solar wind[65–67], consistent with the numerical simulations of the first ionization potential effect on hot coronal loops[57].

While our study does not directly address the formation of magnetic switchbacks, the proton speed and the relative heavy ion speeds reveal properties about the propagation of the switchback. Figure 2b shows that the magnetic field strength is approximately constant inside and outside of the major switchback, but varies at the edges, consistent with observations closer to the Sun[22]. In Fig. 2d, the increase in the radial component of the proton velocity inside the switchback is approximately equal to the local Alfvén speed, both being approximately 50 km s^{-1}, which can be seen from comparing the lines of u_R^p and $u_R^p - u_R^{Alfén}$. Although constant magnetic field strength is not a strict requirement, as shown in ref. 37, these observations are broadly consistent with an outward-propagating large-amplitude spherically polarized Alfvén-like fluctuation[14,36–39,68] and a general feature of switchbacks[15,18,32]. Therefore, magnetic switchbacks propagate at a speed that is approximately the Alfvén speed faster than the bulk flow of the solar wind[69,70].

Heavy ions are observed to drift faster than protons along the magnetic field lines as they escape from the Sun[71–74], and theory suggests that the surplus of momentum is due to resonant absorption of wave momentum[75,76]. The observations in Fig. 2d show that, outside the switchback regions, the heavy ions have a higher speed than the protons, and a slower speed inside the switchback, with both differences in speed (or drift) being near to the local Alfvén speed. The change in sign of the relative drift speed is consistent with multi-ion large-amplitude Alfvén-like fluctuations[77–79]. If the drift speed exceeds the phase speed, which is approximately the Alfvén speed, the plasma can be beam unstable[80–82]. This is also the phase speed of the large-amplitude Alfvén-like fluctuation. These combined effects suggest that the heavy ion populations will travel with the switchback as it propagates away from the Sun. We interpret the Alfvén-like nature as evidence that wave or turbulence mechanisms play a role in the switchback propagation, even when interchange reconnection is the source mechanism[69].

Whether switchbacks require interchange reconnection in the corona remains an open question. We address this in Fig. 2f by presenting signatures of solar source, where we interpret the local increase in

https://doi.org/10.1038/s41550-026-02928-0

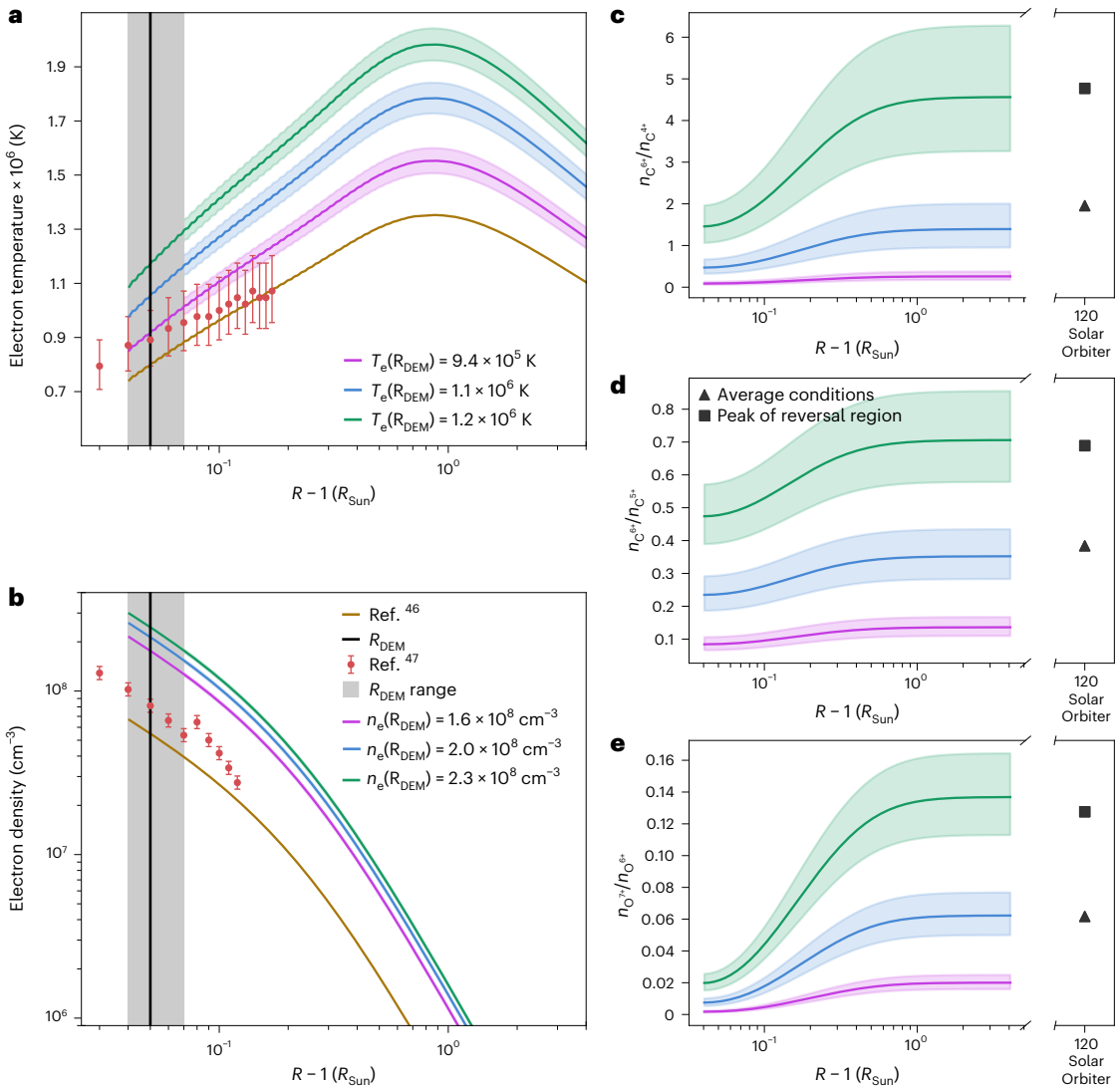


Fig. 4 | An overview of the semi-empirical model of the corona and comparison with the in situ observations by Solar Orbiter. a, The electron temperature. **b**, The electron density. The three coloured lines correspond to characteristic measurements of the most probable values obtained from the DEM method, assumed to be at the R_{DEM}. The shaded regions that encompass the sold lines are propagated from the errors on the measurement and the variation over the day of measurements ('SDO measurements and the DEM' section in Methods). The simulation results[46], observation results[47] and 'R_{DEM} range' labels appear in a shared legend in **b**. In **a** and **b**, the violet, blue and green profiles are the semi-empirical model where the density and temperature values are set at R_{DEM} to the results of the DEM analysis. Right panels: solutions to the non-equilibrium ionization equation for the charge states ('Charge-state ratio evolution in the corona' section in Methods) according to the electron density and temperature profiles. We showed evolution for n_{C6+}/n_{C4+} in **c**, n_{C6+}/n_{C5+} in **d**, and n_{O7+}/n_{O6+} in **e**. The black triangles (squares) are the average conditions of the ion charge-state ratios outside of the switchbacks (peak of the major switchback) measured by Solar Orbiter.

T_e and $n_{O^{7+}}/n_{O^{6+}}$, and decrease in $n_{He^{2+}}/n_p$, as indicators of hot closed-looped magnetic field at the source. These features are evident for the major switchback in Fig. 2, which we interpret as indicators for interchange reconnection as the solar source. It is important to note that the duration of the switchback is long compared with previous studies of the time-duration distribution[19,20,23]. Figure 2f shows high-resolution data for the interval, and it appears that the shorter duration switchbacks have similar signatures to the major switchback, but the local variations are on the order of the combined instrumental noise and statistical standard deviation.

With remote observations of the corona, we further explore the source region to understand the thermodynamics in relation to the enhanced ion charge-state ratio[83–85]. We construct a semi-empirical model of the corona (Fig. 4) that solves for the freeze-in charge-state ratios $n_{O^{7+}}/n_{O^{6+}}$, $n_{C^{6+}}/n_{C^{4+}}$ and $n_{C^{6+}}/n_{C^{5+}}$ given the measured coronal electron temperature and density as lower boundary conditions. This provides evidence for two potential source regions, either the local coronal hole boundary or the coronal hole loops; the latter is indicated by white arrows in Fig. 5. The physical size of the coronal hole loops, being tens of mega-metres and a third of the supergranular size, is consistent with the coronal loops discussed in the solar wind model in ref. 86 where interchange reconnection imparts energy into the corona and releases mass, creating the solar wind (see also refs. 32,87,88).

There are two main sources of error regarding the semi-empirical model. First is the error in the DEM analysis, which we propagate through to the final error. Second, errors could stem from the basic use of model in ref. 46 model. In Supplementary Section 1, we calculate errors based on semi-analytical solutions to the equations in ref. 46. The errors do not cause confusion between source regions for the case

https://doi.org/10.1038/s41550-026-02928-0

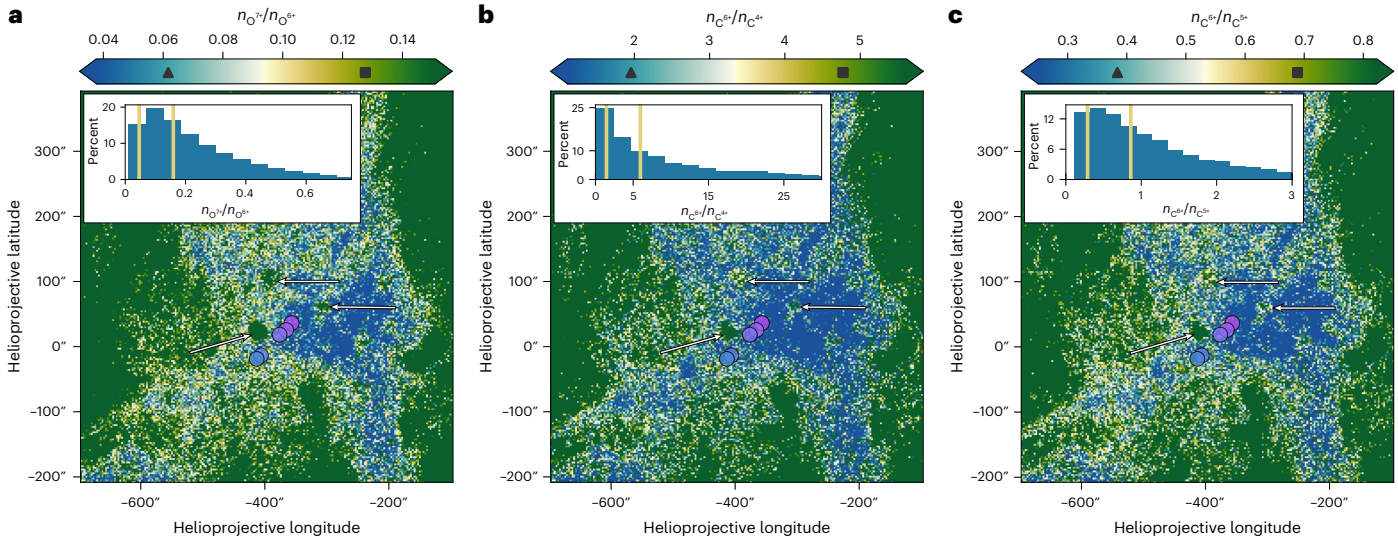


Fig. 5 | The frozen-in charge-state ratio predictions from our semi-empirical model. The method produces an expectation of the frozen-in charge state based on lower boundary conditions supplied by the DEM measurements ('SDO measurements and the DEM' section in Methods) and extrapolation through the corona by solving the non-equilibrium ionization equation with simulation results[46] ('Charge-state ratio evolution in the corona' section in Methods). The plotted colors correspond to expected $n_{O^{7+}}/n_{O^{6+}}$ in **a**, $n_{C^{6+}}/n_{C^{4+}}$ in **b**, and $n_{C^{6+}}/n_{C^{5+}}$ in **c**. The colour bar has been limited by 1.25 times the observed peak of the major switchback and 0.75 times the average conditions of the region outside of the switchbacks. The values of the charge-state ratios of the peak of the major switchback region and average condition appear as squares and triangles on the colour bars. The insets are histograms in units of percent. The vertical yellow lines indicate the range of the colour bars. The three white arrows point to regions of interest discussed in the text. The magnetic footpoint predictions use a source surface height of $2R_{Sun}$, where the colour corresponds with the predictions shown in Fig. 1.

of the peak of the reversal region of the switchback and the average conditions, shown in Fig. 4.

This study indicates that switchbacks are probably a credible link between the solar atmosphere and solar wind, but larger statistical studies, including periods with multiple coronal holes present on-disk and future missions with sophisticated heavy ion instruments, are needed. The case study presented here shows that the switchback retains crucial information on transport from the photosphere into the chromosphere, heating in the corona, energization by kinetic microphysics and propagation away from the Sun. The switchbacks are then likely eroded by reconnection with themselves[89,90] or by strong density gradients[91]. Switchbacks are a demonstration of the fine balance between the two mechanisms for magnetically driven winds (reconnection versus turbulence and waves) and show the elaborate interplay between the two mechanisms[40]. As we build better methods to trace switchbacks and other structures from the photospheric base (where the energy input occurs) to where we observe them, we can make a quantitative determination on the energy transfer mechanisms, in particular to determine the balance between the dichotomy of mechanisms to self-consistently explain coronal heating and solar wind acceleration[1,92].

Methods

The magnetic field model

Figure 1 shows the footpoint predictions of the model described in ref. 41 as squares. The footpoint predictions are generated by sampling an uncertainty ellipse around the target spacecraft position of Solar Orbiter, and then the respective probability densities are remapped across the heliospheric and potential field source surface (PFSS) model. The model information and results are available at ref. 41.

The second set of footpoint predictions, shown as circles, are computed using a coupled PFSS model using the pfsspy package[42] and a Parker Spiral. The input magnetograms used for both models are publicly available at ref. 93.

The magnetic connectivity footpoints of Solar Orbiter shown in Fig. 1 are calculated using a ballistic backmapping method, which employs a PFSS model combined with the Parker spiral approximation. While simple to implement, this approach involves multiple key assumptions that we acknowledge here.

The PFSS model provides static, current-free solutions to the coronal magnetic field using photospheric field data from synoptic magnetograms[94,95]. This yields an idealized minimum-energy field configuration most valid during quiet solar conditions, but it cannot capture dynamic processes such as magnetic reconnection or eruptive events. During our analysed interval, no large-scale eruptions occurred near the coronal hole or were detected in situ at Solar Orbiter.

The model assumes a spherical boundary (the source surface) where field lines become purely radial. In reality, the Alfvén surface probably deviates from spherical geometry, especially during solar maximum when the heliospheric current sheet exhibits complex warping. During March 2022, we are in the ascending phase of the solar cycle with activity levels still relatively low compared with maximum conditions. Since the source surface height provides the biggest uncertainty in the footpoint locations (see, for example, refs. 96,97), we varied this value between 1.5 and 3 solar radii. We found that, for this particular case, varying the source surface height did not drastically alter the connectivity footpoint locations and that during this interval Solar Orbiter is most probably connected to the large equatorial coronal hole. This connection has also been established previously by comparing the in situ solar wind parameters with the remote-sensing observations of the sources[43,98].

While magnetohydrodynamic models that include electric currents and time-dependent phenomena could provide enhanced accuracy, they are computationally expensive and do not necessarily yield drastically different results compared with potential field approaches. Above the source surface, we couple the PFSS solution to a Parker spiral heliospheric model, with spiral geometry determined by the radial velocity measured by Solar Wind Analyser (SWA)/Proton Analyser Sensor (PAS) on board Solar Orbiter. This semi-empirical approach traces field lines from the corona to the spacecraft.

The connectivity points generated by the IRAP tool use radial proton velocities from SWA/PAS during the entire interval between 1 March

2022 18:00 UT and 4 March 2022 00:00 UT, a 24-h window around the observed switchback, during which interval Solar Orbiter detected solar wind with speeds ranging between 396 km s^{-1} to 595 km s^{-1}. The connectivity points calculated from our coupled PFSS and Parker spiral model span the subperiod of investigated (FIg. 1, white bands in the colour bar). We find that the connectivity footpoints from both models congregate in the same region of the large equatorial coronal hole. We also want to emphasize that, rather than determining the precise origin of the switchback, we use the connectivity footpoints from the models as guidance, relying primarily on in situ measurements and the semi-empirical charge-state ratio model to constrain the potential source region.

The highest-probability footpoint prediction of the IRAP model model during the in situ observation time of interest (denoted with vertical white bars in the multi-colour bar) is to an active region near (400″, −100″) in (helioprojective latitude, helioprojective longitude). These are disregarded as the true footpoints because the in situ charge-state ratios (Fig. 2c), except in the magnetic field reversal, are consistent with that of a coronal hole[48,72,99–101]. The charge-state ratios are observed to be low and consistent with a coronal hole for at least a day on either side of the magnetic field reversal[43]. For this reason, we lower the source surface height to $2R_{\mathrm{Sun}}$ to correct for the lack of open magnetic flux that is predicted by the PFSS models with respect to what is inferred from the coronal hole[43]. These results appear as circles in Fig. 1 and are further into the center of the coronal hole. Reference 96 describes a systematic study of the magnetic field connectivity with PFSS models. While the outcome does depend on the interval of interest, they find that the source surface height is the most important parameter in determining the predicted magnetic footpoints.

Our study uses the magnetic connectivity models as guides, and we rely on in situ measurements to constrain our estimation of the true magnetic field footpoints. In our study, we find that the lower source surface height predictions are in a region that matches the predictions of the semi-empirical charge-state ratio model (Figs. 4 and 5) and the in situ charge-state ratio observations of Fig. 2c. The accuracy of magnetic field footpoint estimation through semi-empirical models is an open question that we hope our methods (in particular, Figs. 4 and 5) will help constrain.

In situ measurements of particles and fields

We display in situ particle and magnetic fields measurement in Figs. 2 and 4. Most of the data are publicly available at ref. 102. The O^{7+} measurements and the high-resolution $n_{O^{7+}}/n_{O^{6+}}$ were specifically prepared for this research, and can be obtained from the instrument team[103].

The magnetic field measurements are made by Solar Orbiter's MAG instrument: a pair of fluxgate magnetometers[104]. We use the 'normal mode' data available at eight vectors per second (see table 4 in ref. 104). The magnetic field, in the RTN coordinate system, appears in Fig. 2b. In the RTN system, 'R' radially outwards from the Sun, 'T' is tangent lying in the rotation axis about the Sun and 'N' is orthogonal to 'R' and 'T'.

Solar Orbiter's Solar Wind Analyser (SWA)–Heavy Ion Sensor (HIS) is an electrostatic analyser that isolates incoming ions by energy per charge and direction, being equipped with a time-of-flight telescope and solid-state detectors that measure time of flight and total energy[103,105]. These measurements provide all the information necessary to measure the ion composition, the charge states and their velocity distribution functions. For our study we use the 'normal low cadence' mode data at 10-min cadence (see table 4 in ref. 105 and table 2 in ref. 103) for the charge-state ratios.

The oxygen charge-state number densities of O^{6+} and O^{7+} are large for the interval, so we also use the 'normal mode' data at 30-s time cadence (see table 4 in ref. 105). These measurements appear in Fig. 2f. The counts are summed over the angular dimensions, providing a one-dimensional distribution along the radial direction (that is, 'R' in the RTN coordinate system). Parts of the distribution are removed if the solid-state detector is saturated or if high-energy protons corrupt the signal. The treatment of instrumental noise and artefacts of the one-dimensional velocity distribution functions is described in ref. 103. After this processing, the mean count level of O^{6+} is 277 and O^{7+} is 19, and the mean peak value of O^{6+} is 51 and O^{7+} is 7.

The SWA/PAS is an electrostatic analyser dedicated to measurements of the solar wind protons and He^{2+} velocity distribution functions. We use the 'normal mode' data at 4-s cadence (see table 8 in ref. 105). We remove spurious signals at high energies that are below the noise floor. Since electrostatic analysers measure energy per charge, the proton and He^{2+} populations must be separated (see 'Proton and He^{2+} separation' section in Methods for details on the separation technique).

The SWA Electron Analyser Sensor consists of two electrostatic analysers dedicated to measurements of the solar wind electron distribution functions. We use the 'normal mode' data of 1-s accumulation time every 10 s (see table 8 in ref. 105). We exclude data at low energies (<14 eV), where the electron population is corrupted by interactions with the spacecraft, and high energies (>1,000 eV), where instrument noise is comparable to the signal. To obtain the pitch angle distribution function in Fig. 2a, we average the phase space density over energies from 61 to 1,000 eV and bin-average in 36 pitch angle bins with width of 5°. Figure 2f displays the temperature parameter of the fitted bi-Maxwellian to energies 14–61 eV.

Analysis of particle distribution function measurements

We take moments of the in situ measurements of the proton and heavy ion velocity distribution functions (see 'In situ measurements of particles and fields' section for the density, velocity and temperature[105] and 'Proton and He^{2+} separation' for details on the separation of He^{2+} and protons). The errors of the moments stem from the assumption that the error is a result of finite counting statistics that are Poisson distributed. We propagate this error to the moments of the particle velocity distribution functions. In some cases (for example, Fig. 2d–f), we report the moving average, and so we propagate the counting error and add it to the standard deviation over the moving average time interval.

We write $\langle \ldots \rangle_{100\mathrm{s}}$ to indicate a moving average with a time window of $\tau = 100$ s. We implement the moving average to cancel out noise and retain the local properties. The method we use to produce the time length τ is to set it to half the inverse frequency at which the low-pass-filtered signal is similar to a Gaussian or the noise floor itself.

We use the Jensen–Shannon divergence

$$\mathrm{JSD}(p,q) = \frac{1}{2}\left[D(p||m) + D(p||m)\right], \tag{1}$$

to quantify the similarity of two distributions[106]. Here, p is a histogram of the low-pass-filtered signal. For q, we use two methods: first, a Gaussian with the same mean and standard deviation as p, and second, a high-pass filter on the signal to obtain the measured noise floor. Finally, $m = (p+q)/2$. The divergence is

$$D(p||m) = \sum_{i}^{N} p(b_i) \ln\left|\frac{p(b_i)}{m(b_i)}\right|, \tag{2}$$

where b_i is the bin indexed by i and N is the maximum number of bins. We find this for a large range of bin widths and consequently N, where the results do not change. The quantity $D(p||m)$ is also known as the relative entropy between m and p. The quantity p depends on the choice of the cut-off frequency for the low-pass filter, so we calculate $\mathrm{JSD}(p,q)$ from the smallest frequency to the Nyquist frequency. The quantity $\mathrm{JSD}(p,q)$ sharply decreases at a characteristic frequency that we interpret as the frequency at which the distribution is dominated by noise. We halve the characteristic frequency and use this time scale for the moving average. This provides a method to determine a time scale for the moving

average that preserves properties of the time series and averages out noise. Supplementary Section 2 provides examples of JSD(p, q) on the quantities we report in Fig. 2f.

Proton and He^{2+} separation

We employ the method of ref. 107, which uses the Python package sklearn.mixture included in the scikit-learn library[108], to separate the proton and He^{2+} distribution functions. This method employs Gaussian mixture modelling, where $N = 3$ Gaussian distribution functions are defined and their parameters are updated by an expectation-maximization algorithm until a threshold is satisfied[109]. These distributions provide the probability that an observation belongs to one group or to another. This provides a method to separate the parts of the velocity distribution that belong to the protons and He^{2+}. From these distribution functions, we calculate moments and errors.

The separation of the proton and He^{2+} populations, for an instrument that measures energy per charge, is poor when $\mathbf{u}^{He^{2+}}/\sqrt{2}$ is similar to $\mathbf{u}^{p}$ (where $\mathbf{u}$ is the bulk velocity) because the two velocity distributions overlap. Inside a switchback, the velocity difference ($\mathbf{u}^{He^{2+}} - \mathbf{u}^{p}$) changes sign, which typically causes the overlap to be larger. For the major switchback, in the time interval that we study, the overlap is small and there is no cause for concern. For the short-duration switchbacks, the overlap is larger and the variation of $n_{He^{2+}}/n_p$ is on the order of the error (this is apparent in Fig. 2f). Supplementary Section 3 provides examples of the separation technique.

SDO measurements and the DEM

SDO/AIA is a set of normal-incidence telescopes that image the Sun's electromagnetic emission in the extreme ultraviolet and ultraviolet (UV) ranges[110]. This portion of the spectrum is dominated by emission from coronal ions that permit electron temperature diagnostics in the range of 6×10^4 to 2×10^7 K (ref. 85). The data we use are the six extreme UV passbands obtained during normal observing mode (spatial resolution of 0.6 arcsec and image accumulation time of 10 s (ref. 44)) and are publicly available at ref. 111. We use SDO/AIA and not the Extreme-Ultraviolet Imaging Spectrometer on Hinode as it was not operating, nor the Spectral Imaging of the Coronal Environment, as the field of view was insufficient for our study.

Figure 1 shows the electromagnetic intensity in the 193-Å passband in units of digital number. A measurement of electromagnetic intensity in a single passband is not typically converted to physical units because the results are often unreliable[44]. Instead, one typically obtains information from multiple passbands to derive quantities such as the electron density and temperature. This requires knowledge of the atomic physics and instrument responses. Here, we employ one of many techniques that combine multiple pass bands: the DEM technique[112].

The theory of optically thin plasma in steady-state thermodynamic and collisional–ionization equilibrium dictates that electromagnetic emission intensity is controlled by the electron density and temperature[85,112]. The measured intensity for spectral band b is

$$I_b = \frac{1}{4\pi}\int_0^{+\infty} \mathrm{d}s\, \mathcal{K}_b(T_e) n_e^2 = \int_0^{+\infty} \mathrm{d}T_e \mathcal{K}_b(T_e) \xi(T_e), \tag{3}$$

where s is the line-of-sight dimension (as observed by the instrument), $\mathcal{K}_b$ is the electron temperature (T_e)-dependent response function, which contains the atomic physics of the emission processes and instrument response[113]. The DEM is $\xi = \bar{n}_e^2 \mathrm{d}s/\mathrm{d}T_e$; it is a measure of the amount of emitting plasma, along the line-of-sight dimension, as a function of the electron temperature[113,114]. $\bar{n}_e^2$ is the most probable squared electron density. We use the method of ref. 115, publicly available at ref. 116, to obtain the DEM by solving the inversion of equation (3) by treating it as a least-squares problem and employing regularized singular-value decomposition.

The DEM permits computation of the most probable electron temperature

$$\bar{T}_e = \frac{\int_0^{+\infty} \mathrm{d}T_e\, T_e\, \xi(T_e)}{\int_0^{+\infty} \mathrm{d}T_e\, \xi(T_e)}, \tag{4}$$

and by use of the hydrostatic approximation, a filling factor of unity and assuming $\bar{n}_e^2 = \bar{n}_e^2$, the most probable electron density $\bar{n}_e$

$$\bar{n}_e = \sqrt{\frac{\int_0^{+\infty} \mathrm{d}T_e\, \xi(T_e)}{H}}, \tag{5}$$

where $H = k_B T_e/\mu m_p g$, using the reduced mass $\mu = 0.64$, the proton mass m_p and gravitational acceleration $g = 274$ m s^{-2} (see ref. 117, where these values are applied to an ensemble of coronal holes). More details on the use of the hydrostatic approximation appear in Supplementary Section 1.

The instrument errors are linearly propagated to the DEM, giving $\Delta\xi(T_e)$, and the errors on the temperature derive from the inversion analysis of ref. 115, giving ΔT_e. We linearly propagate these errors to the most probable electron density and temperature for a single 10-s realization. We average the DEM over an entire day surrounding the predicted solar wind release time, and propagate the error to obtain the results shown in Fig. 3. In addition, we set the lower boundary conditions to the averaged $\bar{T}_e$, $\bar{n}_e$ to initialize the semi-empirical model discussed in 'Charge-state ratio evolution in the corona', leading to the results in Figs. 4 and 5.

Charge-state ratio evolution in the corona

Our semi-empirical model extrapolates the electron density and temperature from the low corona, which we assume to be R_{DEM}, into the upper corona (>3R_{Sun}) with the electron density, temperature and the solar wind velocity profiles from ref. 46. The results in ref. 46 are a self-consistent solution to a coronal hole flux tube where the basic inputs are the injected wave power at the lower boundary (the chromosphere) and magnetic field. The model accounts for radiative heating and cooling, electron heat conduction and wave heating. The data are publicly available at ref. 118.

We solve the non-equilibrium ionization equation (spherically symmetric steady-state continuity equation) for element E and charge-state z

$$\begin{aligned}\frac{1}{R^2}\frac{\partial}{\partial R} R^2 n_{E^z} u_{E^z}^R = n_e \big[& n_{E^{z-1}} \mathcal{C}_{E^{z-1}}(T_e) + n_{E^{z+1}} \mathcal{R}_{E^{z+1}}(T_e) \\ & - n_{E^z} \mathcal{C}_{E^z}(T_e) - n_{E^z} \mathcal{R}_{E^z}(T_e) \big],\end{aligned} \tag{6}$$

where the electron temperature T_e, the electron density n_e and the radial component of the velocity $u_{E^z}^R$ are functions of the radial distance R (refs. 49,60). The density, n_{E^z}, is modified by the temperature-dependent recombination $\mathcal{R}_{E^z}(T_e)$ and ionization $\mathcal{C}_{E^z}(T_e)$ rates when the electron density n_e is sufficiently high[119]. We use ionization and recombination rates from the CHIANTI 10.1 database[119] and solve the equation using the method of ref. 120, publicly available at ref. 121. This method produces the charge-state ratios for Figs. 4 and 5.

We scale the functional form of the model results from ref. 46 so that the lower boundary matches the results of our DEM analysis ('SDO measurements and the DEM' section), giving $T_e(R_{DEM}) = \bar{T}_e$, where the right-hand side is the observation (equation (4)) and the left-hand side is the electron temperature profile. We follow the same procedure for the electron density, providing a unique profile for each DEM result. For the speed, we use the model result in ref. 46, which has a final speed of approximately 450 km s^{-1}, consistent with our observations. In Supplementary Section 1, we study semi-analytical solutions to the same equations studied in ref. 46 to derive the temperature, density and speed profiles, to assess errors in our assumptions. We incorporate the

measured deviation in the resulting charge-state ratio and include it in the error analysis, in particular the one that leads to Fig. 4. We discuss this further in Supplementary Section 1.

The R_{DEM} is where the emission intensity of the plasma peaks and is a weak function of electron density and temperature. Here, we assume it is fixed. The possible range we consider is $R_{DEM} = [1.04–1.07]R_{Sun}$ (Fig. 4, grey shading) and consistent with ref. 122. We find that our results (Figs. 4 and 5) are not altered for $R_{DEM} = [1.045–1.06]R_{Sun}$, but outside this range there is poor correspondence between the model predictions of the charge-state ratio and the Solar Orbiter measurements (Fig. 4c–e).

Loop length estimate

In Fig. 5, three areas with white arrows are indicated, where we use the DEM results of electron temperature and density (see 'SDO measurements and the DEM' section) to estimate the coronal loop dimensions[51]. We then compare these results with the approximate size of enhanced charge-state ratio regions in Fig. 5. These indicated internal regions have maximum thermal pressures of $p = (1+\epsilon)n_e k_B T_e = (0.17, 0.23, 0.20)$ dynes cm^{-2} and maximum temperatures of $T_e^{max} = (1.30, 1.36, 1.53) \times 10^6$ K ranked from largest to lowest helioprojective latitude (Fig. 5). Here, $\epsilon = 0.64$ is the fraction of ionized hydrogen. We assume that the hydrogen (or proton) temperature and the electron temperature are equal.

We calculate the loop length $L = 10^9 (T_e^{max}/1.4 \times 10^6)^3 / p$ [cm] using the constant-pressure scaling law[50,52]. These structures are probably coronal bright points[123], and so a filling factor of 0.015 is applied to equation (5) to obtain the loop density[124]. The scaling law then gives loop lengths of $L = (9.50, 7.97, 12.4) \times 10^8$ cm. Assuming they are semi-circular and thus multiplying by 2/π and using an "arcsec" of 7.25×10^7 cm gives diameters of approximately (13, 11, 18) arcsec, ordered from largest to lowest helioprojective latitude (Fig. 5).

Data availability

The sources of the observational data shown in this article are reported in the relevant Methods sections. The Solar Orbiter data are available via ESA at https://soar.esac.esa.int/soar/ (ref. 102). All data are publicly available except for some observational data described in 'In situ measurements of particles and fields' in Methods, where instructions on how to obtain the data are described. The magnetic field modelling requires magnetogram measurements that are publicly available via NSO at https://gong.nso.edu/adapt/maps/. The DEM requires spectral emission data that are publicly available at https://sdo.gsfc.nasa.gov/. The semi-empirical model uses results from a numerical simulation in ref. 46 which are available via Bitbucket at https://stevencranmer.bitbucket.io/Data/Zephyr2007/.

Code availability

The codes used for analysis in this article are reported in the relevant Methods sections. To model the heavy ions in the corona, we use the Fiasco code[120]. To model the magnetic field, we use the Pfsspy code[42]. To separate the proton and He^{2+} populations, we use the Scikit-learn code[108].

References

1. Cranmer, S. R. Coronal holes. *Living Rev. Sol. Phys.* **6**, 3 (2009).
2. West, M. J. et al. Defining the middle corona. *Sol. Phys.* **298**, 78 (2023).
3. Müller, D. et al. The Solar Orbiter mission. *Astron. Astrophys.* **642**, A1 (2020).
4. Moldwin, M. B., Ford, S., Lepping, R., Slavin, J. & Szabo, A. Small scale magnetic flux ropes in the solar wind. *Geophys. Res. Lett.* **27**, 57–60 (2000).
5. Choi, K.-E. et al. Characteristics of suprathermal electrons in small-scale magnetic flux ropes and their implications on the magnetic connection to the sun. *Sol. Phys.* **296**, 1–24 (2021).
6. Zhai, C., Fu, H., Si, J., Huang, Z. & Xia, L. The properties of small magnetic flux ropes inside the solar wind come from coronal holes, active regions, and quiet sun. *Astrophys. J.* **950**, 79 (2023).
7. Crooker, N. U., Gosling, J. T. & Kahler, S. W. Reducing heliospheric magnetic flux from coronal mass ejections without disconnection. *J. Geophys. Res. Space Phys.* **107**, SSH 3–1–SSH 3–5 (2002).
8. Fisk, L. A. & Kasper, J. C. Global circulation of the open magnetic flux of the Sun. *Astrophys. J. Lett.* **894**, L4 (2020).
9. Gosling, J. T. Coronal mass ejections and magnetic flux ropes in interplanetary space. *Phys. Magn. Flux Ropes* **58**, 343–364 (1990).
10. Hundhausen, A. *An Interplanetary View of Coronal Holes* (Colorado Associated Univ. Press, 1977).
11. Ness, N. F., Scearce, C. S. & Cantarano, S. Preliminary results from the Pioneer 6 Magnetic Field Experiment. *J. Geophys. Res.* **71**, 3305–3313 (1966).
12. Owens, M. J. & Forsyth, R. J. The heliospheric magnetic field. *Living Rev. Sol. Phys.* **10**, 5 (2013).
13. Balogh, A., Forsyth, R. J., Lucek, E. A., Horbury, T. S. & Smith, E. J. Heliospheric magnetic field polarity inversions at high heliographic latitudes. *Geophys. Res. Lett.* **26**, 631–634 (1999).
14. Gosling, J. T., McComas, D. J., Roberts, D. A. & Skoug, R. M. A one-sided aspect of the Alfvénic fluctuations in the solar wind. *Astrophys. J.* **695**, L213–L216 (2009).
15. Matteini, L., Horbury, T. S., Neugebauer, M. & Goldstein, B. E. Dependence of solar wind speed on the local magnetic field orientation: role of Alfvénic fluctuations. *Geophys. Res. Lett.* **41**, 259–265 (2014).
16. Kasper, J. C. et al. Alfvénic velocity spikes and rotational flows in the near-Sun solar wind. *Nature* **576**, 228–231 (2019).
17. Bale, S. D. et al. Highly structured slow solar wind emerging from an equatorial coronal hole. *Nature* **576**, 237–242 (2019).
18. Horbury, T. S. et al. Sharp Alfvénic impulses in the near-sun solar wind. *Astrophys. J. Suppl. Ser.* **246**, 45 (2020).
19. Larosa, A. et al. Switchbacks: statistical properties and deviations from Alfvénicity. *Astron. Astrophys.* **650**, A3 (2021).
20. Tenerani, A. et al. Evolution of switchbacks in the inner heliosphere. *Astrophys. J. Lett.* **919**, L31 (2021).
21. Jagarlamudi, V. K. et al. Occurrence and evolution of switchbacks in the inner heliosphere: Parker Solar Probe observations. *Astrophys. J. Lett.* **950**, L7 (2023).
22. Huang, J. et al. The structure and origin of switchbacks: Parker Solar Probe observations. *Astrophys. J.* **952**, 33 (2023).
23. Dudok de Wit, T. et al. Switchbacks in the near-sun magnetic field: long memory and impact on the turbulence cascade. *Astrophys. J. Suppl. Ser.* **246**, 39 (2020).
24. Fargette, N. et al. Characteristic scales of magnetic switchback patches near the sun and their possible association with solar supergranulation and granulation. *Astrophys. J.* **919**, 96 (2021).
25. Mozer, F. S. et al. On the origin of switchbacks observed in the solar wind. *Astrophys. J.* **919**, 60 (2021).
26. Bale, S. D. et al. A solar source of Alfvénic magnetic field switchbacks: in situ remnants of magnetic funnels on supergranulation scales. *Astrophys. J.* **923**, 174 (2021).
27. Perrone, D. et al. Solar orbiter observations of proton and alpha particle kinetic signatures related to the presence of switchbacks in the inner heliosphere: a case study. *Astrophys. J.* **973**, 171 (2024).
28. Rivera, Y. J. et al. Mixed source region signatures inside magnetic switchback patches inferred by heavy ion diagnostics. *Astrophys. J.* **974**, 198 (2024).
29. Zank, G. P., Nakanotani, M., Zhao, L.-L., Adhikari, L. & Kasper, J. The origin of switchbacks in the solar corona: linear theory. *Astrophys. J.* **903**, 1 (2020).

30. Drake, J. F. et al. Switchbacks as signatures of magnetic flux ropes generated by interchange reconnection in the corona. *Astron. Astrophys.* **650**, A2 (2021).
31. He, J. et al. Solar origin of compressive Alfvénic spikes/kinks as observed by Parker Solar Probe. *Astrophys. J. Lett.* **913**, L14 (2021).
32. Bale, S. D. et al. Interchange reconnection as the source of the fast solar wind within coronal holes. *Nature* **618**, 252–256 (2023).
33. Agapitov, O. V. et al. Flux rope merging and the structure of switchbacks in the solar wind. *Astrophys. J.* **925**, 213 (2022).
34. Gannouni, B., Réville, V. & Rouillard, A. P. Modeling the formation and evolution of solar wind microstreams: from coronal plumes to propagating Alfvénic velocity spikes. *Astrophys. J.* **958**, 110 (2023).
35. Ruffolo, D. et al. Shear-driven transition to isotropically turbulent solar wind outside the Alfvén critical zone. *Astrophys. J.* **902**, 94 (2020).
36. Squire, J., Chandran, B. D. G. & Meyrand, R. In-situ switchback formation in the expanding solar wind. *Astrophys. J. Lett.* **891**, L2 (2020).
37. Mallet, A., Squire, J., Chandran, B. D. G., Bowen, T. & Bale, S. D. Evolution of large-amplitude Alfvén waves and generation of switchbacks in the expanding solar wind. *Astrophys. J.* **918**, 62 (2021).
38. Shoda, M., Chandran, B. D. G. & Cranmer, S. R. Turbulent generation of magnetic switchbacks in the Alfvénic solar wind. *Astrophys. J.* **915**, 52 (2021).
39. Toth, G., Velli, M. & Holst, B. v. d. Theory of magnetic switchbacks fully supported by Parker Solar Probe observations. *Astrophys. J.* **957**, 95 (2023).
40. Raouafi, N. E. et al. Parker Solar Probe: four years of discoveries at solar cycle minimum. *Space Sci. Rev.* **219**, 8 (2023).
41. Rouillard, A. P. et al. Models and data analysis tools for the Solar Orbiter mission. *Astron. Astrophys.* **642**, A2 (2020).
42. Stansby, D., Yeates, A. & Badman, S. T. pfsspy: a python package for potential field source surface modelling. *J. Open Source Softw.* **5**, 2732 (2020).
43. Yardley, S. L. et al. Multi-source connectivity as the driver of solar wind variability in the heliosphere. *Nat. Astron.* **8**, 953–963 (2024).
44. Boerner, P. et al. Initial calibration of the Atmospheric Imaging Assembly (AIA) on the Solar Dynamics Observatory (SDO). *Sol. Phys.* **275**, 41–66 (2012).
45. Landi, E., Gruesbeck, J. R., Lepri, S. T. & Zurbuchen, T. H. New solar wind diagnostic using both in situ and spectroscopic measurements. *Astrophys. J.* **750**, 159 (2012).
46. Cranmer, S. R., Ballegooijen, A. A. V. & Edgar, R. J. Self-consistent coronal heating and solar wind acceleration from anisotropic magnetohydrodynamic turbulence. *Astrophys. J. Suppl. Ser.* **171**, 520 (2007).
47. Landi, E. The off-disk thermal structure of a polar coronal hole. *Astrophys. J.* **685**, 1270–1276 (2008).
48. Hundhausen, A. J., Gilbert, H. E. & Bame, S. J. The state of ionization of oxygen in the solar wind. *Astrophys. J.* **152**, L3 (1968).
49. Owocki, S. P., Holzer, T. E. & Hundhausen, A. J. The solar wind ionization state as a coronal temperature diagnostic. *Astrophys. J.* **275**, 354 (1983).
50. Rosner, R., Tucker, W. H. & Vaiana, G. S. Dynamics of the quiescent solar corona. *Astrophys. J.* **220**, 643 (1978).
51. Porter, L. J. & Klimchuk, J. A. Soft X-ray loops and coronal heating. *Astrophys. J.* **454**, 499 (1995).
52. Reale, F. Coronal loops: observations and modeling of confined plasma. *Living Rev. Sol. Phys.* **11**, 4 (2014).
53. Landi, E. et al. Carbon ionization stages as a diagnostic of the solar wind. *Astrophys. J.* **744**, 100 (2012).
54. Geiss, J., Hirt, P. & Leutwyler, H. On acceleration and motion of ions in corona and solar wind. *Sol. Phys.* **12**, 458–483 (1970).
55. Hollweg, J. V. Resonances of coronal loops. *Astrophys. J.* **277**, 392 (1984).
56. Schwadron, N. A., Fisk, L. A. & Zurbuchen, T. H. Elemental fractionation in the slow solar wind. *Astrophys. J.* **521**, 859–867 (1999).
57. Rakowski, C. E. & Laming, J. M. On the origin of the slow speed solar wind: helium abundance variations. *Astrophys. J.* **754**, 65 (2012).
58. Laming, J. M. The FIP and inverse FIP effects in solar and stellar coronae. *Living Rev. Sol. Phys.* **12**, 2 (2015).
59. Réville, V. et al. Investigating the origin of the first ionization potential effect with a shell turbulence model. *Front. Astron. Space Sci.* **8**, 619463 (2021).
60. Rivera, Y. J. et al. Deciphering the birth region, formation, and evolution of ambient and transient solar wind using heavy ion observations. *Front. Astron. Space Sci.* **9**, 1056347 (2022).
61. Priest, E. R. The structure of coronal loops. *Sol. Phys.* **58**, 57–87 (1978).
62. Priest, E. R. et al. A method to determine the heating mechanisms of the solar corona. *Astrophys. J.* **539**, 1002–1022 (2000).
63. Sharma, R. & Morton, R. J. Transverse energy injection scales at the base of the solar corona. *Nat. Astron.* **7**, 1301–1308 (2023).
64. Laming, J. M. & Feldman, U. The variability of the solar coronal helium abundance: polar coronal holes compared to the quiet sun. *Astrophys. J.* **591**, 1257–1266 (2003).
65. Kasper, J. C., Stevens, M. L., Lazarus, A. J., Steinberg, J. T. & Ogilvie, K. W. Solar wind helium abundance as a function of speed and heliographic latitude: variation through a solar cycle. *Astrophys. J.* **660**, 901–910 (2007).
66. Alterman, B. & D'Amicis, R. Cross helicity and the helium abundance as an in situ metric of solar wind acceleration. *Astrophys. J. Lett.* **982**, L40 (2025).
67. Rivera, Y. J. et al. Differentiating the acceleration mechanisms in the slow and Alfvénic slow solar wind. *Astrophys. J.* **980**, 70 (2025).
68. Barnes, A. & Hollweg, J. V. Large amplitude hydromagnetic waves. *J. Geophys. Res.* **79**, 2302–2318 (1974).
69. Wyper, P. F. et al. The imprint of intermittent interchange reconnection on the solar wind. *Astrophys. J. Lett.* **941**, L29 (2022).
70. Lionello, R. et al. Global mhd simulations of the time-dependent corona. *Astrophys. J.* **959**, 77 (2023).
71. Abraham Shrauner, B. & Feldman, W. C. Nonlinear Alfvén waves in high speed solar wind streams. *J. Geophys. Res.* **82**, 618–624 (1977).
72. Bochsler, P. Minor ions in the solar wind. *Astron. Astrophys. Rev.* **14**, 1–40 (2007).
73. Berger, L., Wimmer-Schweingruber, R. F. & Gloeckler, G. Systematic measurements of ion-proton differential streaming in the solar wind. *Phys. Rev. Lett.* **106**, 151103 (2011).
74. Tracy, P. J. et al. Constraining solar wind heating processes by kinetic properties of heavy ions. *Phys. Rev. Lett.* **116**, 255101 (2016).
75. Isenberg, P. A. & Hollweg, J. V. On the preferential acceleration and heating of solar wind heavy ions. *J. Geophys. Res.: Space Phys.* **88**, 3923–3935 (1983).
76. Cranmer, S. R. Coronal holes and the high-speed solar wind. *Space Sci. Rev.* **101**, 229–294 (2002).
77. Matteini, L., Horbury, T. S., Pantellini, F., Velli, M. & Schwartz, S. J. Ion kinetic energy conservation and magnetic field strength constancy in multi-fluid solar wind Alfvénic turbulence. *Astrophys. J.* **802**, 11 (2015).
78. Woolley, T. et al. Plasma properties, switchback patches, and low α-particle abundance in slow Alfvénic coronal hole wind at 0.13 au. *Mon. Not. R. Astron. Soc.* **508**, 236–244 (2021).
79. McManus, M. D. et al. Density and velocity fluctuations of alpha particles in magnetic switchbacks. *Astrophys. J.* **933**, 43 (2022).

80. Asbridge, J. R., Bame, S. J., Feldman, W. C. & Montgomery, M. D. Helium and hydrogen velocity differences in the solar wind. *J. Geophys. Res.* **81**, 2719–2727 (1976).
81. Marsch, E., Mühlhäuser, K., Rosenbauer, H., Schwenn, R. & Neubauer, F. M. Solar wind helium ions: observations of the Helios solar probes between 0.3 and 1 AU. *J. Geophys. Res. Space Phys.* **87**, 35–51 (1982).
82. Verscharen, D., Bourouaine, S. & Chandran, B. D. G. Instabilities driven by the drift and temperature anisotropy of alpha particles in the solar wind. *Astrophys. J.* **773**, 163 (2013).
83. Newkirk, J. G. Structure of the solar corona. *Annu. Rev. Astron. Astrophys.* **5**, 213–266 (1967).
84. Mason, H. E. & Fossi, B. C. M. Spectroscopic diagnostics in the VUV for solar and stellar plasmas. *Astron. Astrophys. Rev.* **6**, 123–179 (1994).
85. Del Zanna, G. & Mason, H. E. Solar UV and X-ray spectral diagnostics. *Living Rev. Sol. Phys.* **15**, 5 (2018).
86. Fisk, L. A. Acceleration of the solar wind as a result of the reconnection of open magnetic flux with coronal loops. *J. Geophys. Res.: Space Phys.* **108**, A4 (2003).
87. Fazakerley, A. N., Harra, L. K. & Driel-Gesztelyi, L. V. An investigation of the sources of Earth-directed solar wind during Carrington rotation 2053. *Astrophys. J.* **823**, 145 (2016).
88. Raouafi, N. E. et al. Magnetic reconnection as the driver of the solar wind. *Astrophys. J.* **945**, 28 (2023).
89. Fedorov, A. et al. Switchback-like structures observed by Solar Orbiter. *Astron. Astrophys.* **656**, A40 (2021).
90. Suen, G. H. H. et al. Magnetic reconnection as an erosion mechanism for magnetic switchbacks. *Astron. Astrophys.* **675**, A128 (2023).
91. Tenerani, A. et al. Magnetic field kinks and folds in the solar wind. *Astrophys. J. Suppl. Ser.* **246**, 32 (2020).
92. Rivera, Y. J. et al. In situ observations of large-amplitude Alfvén waves heating and accelerating the solar wind. *Science* **385**, 962–966 (2024).
93. Arge, C. N. et al. Air Force Data Assimilative Photospheric Flux Transport (ADAPT) model. *AIP Conf. Proc.* **1216**, 343–346 (2010).
94. Altschuler, M. D. & Newkirk Jr, G. Magnetic fields and the structure of the solar corona: I: methods of calculating coronal fields. *Sol. Phys.* **9**, 131–149 (1969).
95. Schatten, K. H., Wilcox, J. M. & Ness, N. F. A model of interplanetary and coronal magnetic fields. *Sol. Phys.* **6**, 442–455 (1969).
96. Bizien, N., Froment, C., Madjarska, M. S., de Wit, T. D. & Velli, M. Tracing magnetic switchbacks to their source: an assessment of solar coronal jets as switchback precursors. *Astron. Astrophys.* **694**, A181 (2025).
97. Koukras, A., Dolla, L. & Keppens, R. Estimating uncertainties in the back-mapping of the fast solar wind. *Astron. Astrophys.* **694**, A134 (2025).
98. Yardley, S. L. et al. Slow solar wind connection science during solar orbiter's first close perihelion passage. *Astrophys. J. Suppl. Ser.* **267**, 11 (2023).
99. Geiss, J., Gloeckler, G. & Steiger, R. V. Origin of the solar wind from composition data. *Space Sci. Rev.* **72**, 49–60 (1995).
100. Gloeckler, G., Zurbuchen, T. H. & Geiss, J. Implications of the observed anticorrelation between solar wind speed and coronal electron temperature. *J. Geophys. Res. Space Phys.* **108**, A4 (2003).
101. Schwadron, N. A. et al. Solar wind from the coronal hole boundaries. *J. Geophys. Res. Space Phys.* **110**, A4 (2005).
102. Solar Orbital archive. *European Space Agency* http://soar.esac.esa.int/soar/ (n.d.).
103. Livi, S. et al. First results from the Solar Orbiter Heavy Ion Sensor. *Astron. Astrophys.* **676**, A36 (2023).
104. Horbury, T. S. et al. The Solar Orbiter magnetometer. *Astron. Astrophys.* **642**, A9 (2020).
105. Owen, C. J. et al. The Solar Orbiter Solar Wind Analyser (SWA) suite. *Astron. Astrophys.* **642**, A16 (2020).
106. Briët, J. & Harremoës, P. Properties of classical and quantum Jensen-Shannon divergence. *Phys. Rev. A* **79**, 052311 (2009).
107. De Marco, R. et al. Innovative technique for separating proton core, proton beam, and alpha particles in solar wind 3D velocity distribution functions. *Astron. Astrophys.* **669**, A108 (2023).
108. Pedregosa, F. et al. scikit-learn: machine learning in python. *J. Mach. Learn. Res.* **12**, 2825–2830 (2011).
109. Dempster, A. P., Laird, N. M. & Rubin, D. B. Maximum likelihood from incomplete data via the EM algorithm. *J. R. Stat. Soc. Ser. B* **39**, 1–22 (1977).
110. Lemen, J. R. et al. The Atmospheric Imaging Assembly (AIA) on the Solar Dynamics Observatory (SDO). *Sol. Phys.* **275**, 17–40 (2012).
111. Solar Dynamics Observatory. *NASA* http://sdo.gsfc.nasa.gov/ (n.d.).
112. Mariska, J. T. *The Solar Transition Region* (Cambridge Univ. Press, 1992).
113. Guennou, C. et al. On the accuracy of the differential emission measure diagnostics of solar plasmas. Application to SDO/AIA. I. Isothermal plasmas. *Astrophys. J. Suppl. Ser.* **203**, 25 (2012).
114. Pottasch, S. R. On the interpretation of the solar ultraviolet emission line spectrum. *Space Sci. Rev.* **3**, 816–855 (1964).
115. Hannah, I. G. & Kontar, E. P. Differential emission measures from the regularized inversion of Hinode and SDO data. *Astron. Astrophys.* **539**, A146 (2012).
116. Hannah, I. Calculate the Differential Emission Measure (DEM) from solar data using regularised inversion. *GitHub* https://github.com/ianan/demreg (n.d.).
117. Heinemann, S. G., Saqri, J., Veronig, A. M., Hofmeister, S. J. & Temmer, M. Statistical approach on differential emission measure of coronal holes using the CATCH catalog. *Sol. Phys.* **296**, 18 (2021).
118. Cranmer, S.R. Codes and data. *Bitbucket* http://stevencranmer.bitbucket.io/cranmer_data.html (n.d.).
119. Dere, K. P., Zanna, G. D., Young, P. R. & Landi, E. CHIANTI—an atomic database for emission lines. XVII. Version 10.1: revised ionization and recombination rates and other updates, released on 2023 July 17. *Astrophys. J. Suppl. Ser.* **268**, 52 (2023).
120. Barnes, W. et al. wtbarnes/fiasco: v0.2.3. *Zenodo* https://doi.org/10.5281/zenodo.10612118 (2024).
121. Barnes, W. Python interface to the CHIANTI atomic database. *GitHub* https://github.com/wtbarnes/fiasco (n.d.).
122. Yang, S. H., Zhang, J., Jin, C. L., Li, L. P. & Duan, H. Y. Response of the solar atmosphere to magnetic field evolution in a coronal hole region. *Astron. Astrophys.* **501**, 745–753 (2009).
123. Madjarska, M. S. Coronal bright points. *Living Rev. Sol. Phys.* **16**, 2 (2019).
124. Dere, K. P. The plasma filling factor of coronal bright points. *Astron. Astrophys.* **497**, 287–290 (2009).

Acknowledgements

J.T.C. thanks W. Wright for support during this project.

Author contributions

J.T.C.: project planning, data analysis and primary writing of the article. S.L.Y.: project planning and data analysis. N.N.: project planning and data analysis. R.D.: project planning, contributions to experimental work, and data analysis. Y.J.R.: numerical methods. R.D.M.: data analysis. D.V.: project planning and contributions to experimental work. C.J.O.: project planning and contributions to experimental work. G.H.H.S.: data analysis. B.A.: contributions to experimental

work. D.B.: project planning. A.F.: project planning and contributions to experimental work. A.B.G.: contributions to experimental work. J.H.: project planning. T.S.H.: contributions to experimental work. C.H.: project planning. C.I.: data analysis. L.M.K.: contributions to experimental work. S.T.L.: contributions to experimental work. S.L.: contributions to experimental work. P.L.: contributions to experimental work. G.N.: data analysis and contributions to experimental work. J.M.R.: contributions to experimental work. A.P.R.: contributions to experimental work.

Funding

J.T.C., D.V. and C.J.O. were supported by UKRI grants ST/W001004/1 and UKRI1204. S.L.Y. acknowledge the Science Technology and Facilities Council for the award of an Ernest Rutherford Fellowship (ST/X003787/1). N.N. was supported by STFC PhD studentship grant ST/W507891/1 and UCL Studentship during his PhD education at UCL. The SWA-HIS team acknowledges NASA contract NNG10EK25C. R.D. is supported by the INAF 2023 Fundamental Research grant 'Machine Learning on Solar Wind Velocity Distribution Functions'. G.H.H.S. is partially supported by the Royal Society (UK) and the Consiglio Nazionale delle Ricerche (Italy) through the International Exchanges Cost Share scheme/Joint Bilateral Agreement project 'Multi-scale electrostatic energisation of plasmas: comparison of collective processes in laboratory and space' (award nos. IEC R2 222050 and SAC.AD002.043.021). G.H.H.S. also acknowledges funding from the CEFIPRA research project no. 6904-2 and the financial support of the Centre National d'Études Spatiales (CNES) through its APR programme. B.L.A. acknowledges NASA grant 80NSSC22K1011 (LWS) along with Solar Orbiter funding at NASA Goddard Space Flight Center. D.B. acknowledge support from UKSA grant nos. UKRI920 and UKRI980. UNH funding under subcontract A99200MO under NASA NNG10EK25C. Solar Orbiter magnetometer operations are funded by the UK Space Agency (grant no. UKRI943). T.S.H. is supported by STFC grant UKRI1202. C.H. is supported by the Alexander von Humboldt Foundation. The work carried out at the Leibniz-Institut für Astrophysik Potsdam by A.P.R. was supported by the Alexander von Humboldt foundation. The Magnetic Connectivity Tool[41] is developped by the Solar-Terrestrial Observations and Modelling Service; STORMS; https://stormsweb.irap.omp.eu/). Solar Orbiter is a mission of international cooperation between ESA and NASA, operated by ESA. Solar Orbiter SWA data were derived from scientific sensors that were designed and created and are operated under funding provided by numerous contracts from UKSA, STFC, the Italian Space Agency, CNES, the French National Centre for Scientific Research, the Czech contribution to the ESA PRODEX programme and NASA. Solar Orbiter SWA operations at the UCL/Mullard Space Science Laboratory were funded by UKRI grant nos. ST/X002152/1 and UKRI919.

Competing interests

The authors declare no competing interests.

Additional information

Supplementary information The online version contains supplementary material available at https://doi.org/10.1038/s41550-026-02928-0.

Correspondence and requests for materials should be addressed to Jesse T. Coburn.

Peer review information *Nature Astronomy* thanks the anonymous reviewers for their contribution to the peer review of this work.

Reprints and permissions information is available at www.nature.com/reprints.

Publisher's note Springer Nature remains neutral with regard to jurisdictional claims in published maps and institutional affiliations.

Open Access This article is licensed under a Creative Commons Attribution 4.0 International License, which permits use, sharing, adaptation, distribution and reproduction in any medium or format, as long as you give appropriate credit to the original author(s) and the source, provide a link to the Creative Commons licence, and indicate if changes were made. The images or other third party material in this article are included in the article's Creative Commons licence, unless indicated otherwise in a credit line to the material. If material is not included in the article's Creative Commons licence and your intended use is not permitted by statutory regulation or exceeds the permitted use, you will need to obtain permission directly from the copyright holder. To view a copy of this licence, visit http://creativecommons.org/licenses/by/4.0/.

© The Author(s) 2026

[1]Mullard Space Science Laboratory, Department of Space and Climate Physics, University College London, Holmbury St. Mary, UK. [2]Laboratoire de Physique des Plasmas, CNRS, Observatoire de Paris, Sorbonne Université, Université Paris Saclay, École polytechnique, Institut Polytechnique de Paris, Palaiseau, France. [3]Department of Mathematics, Physics and Electrical Engineering, Northumbria University, Newcastle, UK. [4]Donostia International Physics Center, San Sebastián, Spain. [5]Solar System Research, Max Planck Institute, Göttingen, Germany. [6]Climate and Space Sciences and Engineering, Climate and Space Research, University of Michigan, Ann Arbor, MI, USA. [7]Center for Astrophysics, Harvard & Smithsonian, Cambridge, MA, USA. [8]Istituto di Astrofisica e Planetologia Spaziale, Rome, Italy. [9]LPC2E, OSUC, University of Orleans, CNRS, CNES, Orleans, France. [10]Heliophysics Science Division, NASA Goddard Space Flight Center, Greenbelt, MD, USA. [11]Institute for the Study of Earth, Oceans, and Space and the Department of Physics and Astronomy, University of New Hampshire, Durham, NH, USA. [12]School of Earth and Space Sciences, Peking University, Beijing, P.R. China. [13]Department of Physics, Imperial College, London, UK. [14]Institut für Physik und Astronomie, Universität Potsdam, Potsdam, Germany. [15]Space Science, Southwest Research Institute, San Antonio, TX, USA. [16]Institut de Recherche en Astrophysique et Planétologie, Université Toulouse, Toulouse, France. [17]University Toulouse, CNES, CNRS, IRAP, Toulouse, France. [18]Leibniz-Institut für Astrophysik Potsdam, Potsdam, Germany.
✉e-mail: jesse.coburn@lpp.polytechnique.fr